Automatic Aorta Segmentation and Valve Landmark Detection in C-Arm CT for Transcatheter Aortic Valve Implantation

Yefeng Zheng*, *Senior Member, IEEE*, Matthias John, Rui Liao, *Senior Member, IEEE*, Alois Nöttling, Jan Boese, Jörg Kempfert, Thomas Walther, Gernot Brockmann, and Dorin Comaniciu, *Fellow, IEEE*

Abstract—Transcatheter aortic valve implantation (TAVI) is a minimally invasive procedure to treat severe aortic valve stenosis. As an emerging imaging technique, C-arm computed tomography (CT) plays a more and more important role in TAVI on both pre-operative surgical planning (e.g., providing 3-D valve measurements) and intra-operative guidance (e.g., determining a proper C-arm angulation). Automatic aorta segmentation and aortic valve landmark detection in a C-arm CT volume facilitate the seamless integration of C-arm CT into the TAVI workflow and improve the patient care. In this paper, we present a part-based aorta segmentation approach, which can handle structural variation of the aorta in case that the aortic arch and descending aorta are missing in the volume. The whole aorta model is split into four parts: aortic root, ascending aorta, aortic arch, and descending aorta. Discriminative learning is applied to train a detector for each part separately to exploit the rich domain knowledge embedded in an expert-annotated dataset. Eight important aortic valve landmarks (three hinges, three commissures, and two coronary ostia) are also detected automatically with an efficient hierarchical approach. Our approach is robust under all kinds of variations observed in a real clinical setting, including changes in the field-of-view, contrast agent injection, scan timing, and aortic valve regurgitation. Taking about 1.1 s to process a volume, it is also computationally efficient. Under the guidance of the automatically extracted patient-specific aorta model, the physicians can properly determine the C-arm angulation and deploy the prosthetic valve. Promising outcomes have been achieved in real clinical applications.

Index Terms—Aorta segmentation, aortic valve landmark detection, C-arm computed tomography (CT), transcatheter aortic valve implantation, transcatheter aortic valve replacement.

I. INTRODUCTION

THE open-heart aortic valve replacement is an effective method to treat severe aortic valve disease. With 50 000 procedures performed annually, it is the most common valvular heart surgery in the United States [1]. However, at least 30% of patients cannot tolerate the surgical trauma due to the advanced age or the presence of various comorbidities [2]. Transcatheter aortic valve implantation (TAVI) [also known as transcatheter aortic valve replacement (TAVR)] is an emerging, less invasive procedure to treat severe aortic valve stenosis, where the prosthetic valve is inserted and deployed using a catheter through a small puncture of the femoral artery (the transfemoral approach) or a small cut at the heart apex (the transapical approach). After the first in-human TAVI case performed in 2002, the procedure has been adopted rapidly, especially after the approval for commercial use in Europe in 2007, with more than 30 000 TAVI procedures performed in the world so far [3]. TAVI has already accounted for more than 20% of aortic valve replacement procedures in Germany [4]. It is expected to grow fast in the United States too after the recent approval for commercial use in November 2011. The recent randomized trials show that TAVI significantly reduces the mortality rate for a patient who is too sick or weak to be a candidate for surgical valve replacement, compared to the current standard medical therapy [2]. For a high-risk patient who can still tolerate the surgical valve replacement, TAVI has comparable outcomes to the open-heart surgical procedure [5].

Before the TAVI procedure, several important parameters of the aortic valve (see Fig. 1 for the aortic valve anatomy) need to be measured for surgical planning. For example, the distance between the coronary ostia and the aortic valve hinge plane (the lowest level of the valve cusps) is a critical parameter for patient selection since a short distance increases the risk of blocking coronary circulation after valve deployment. The diameter of aortic valve annulus needs to be measured accurately to select a prosthetic valve with an appropriate size. Fluoroscopy is currently the main working-horse imaging modality for TAVI (see Fig. 2), where real-time images are captured on a C-arm system to provide guidance to physicians [6]. The aortic root structure is normally indistinguishable from the background [Fig. 2(c)]; therefore, whenever necessary, the contrast agent is applied to temporarily enhance the valve structure [Fig. 2(b)] for a short period. However, the contrast agent is toxic and its usage should
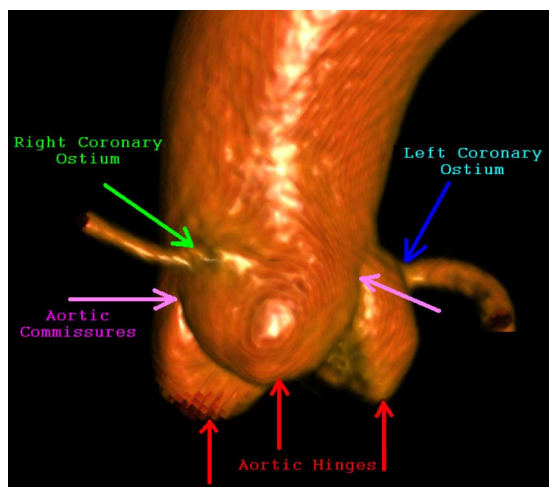
Fig. 1. Anatomy of the aortic valve with aortic hinges indicated by red arrows, aortic commissures indicated by purple arrows, and left/right coronary ostium indicated by the green/blue arrow, respectively. Note: The third aortic commissure is at the back of the valve and blocked in this view.
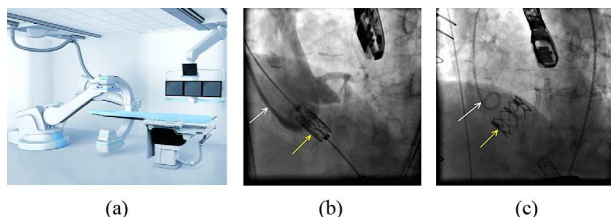

Fig. 2. Transapical aortic valve implantation under X-ray guidance. (a) An angiographic C-arm system able to acquire interventional 3-D CT images in an operating room. (b) Contrast injection via a pigtail catheter (the white arrow) immediately prior to valve (the yellow arrow) deployment. (c) Implanted valve.
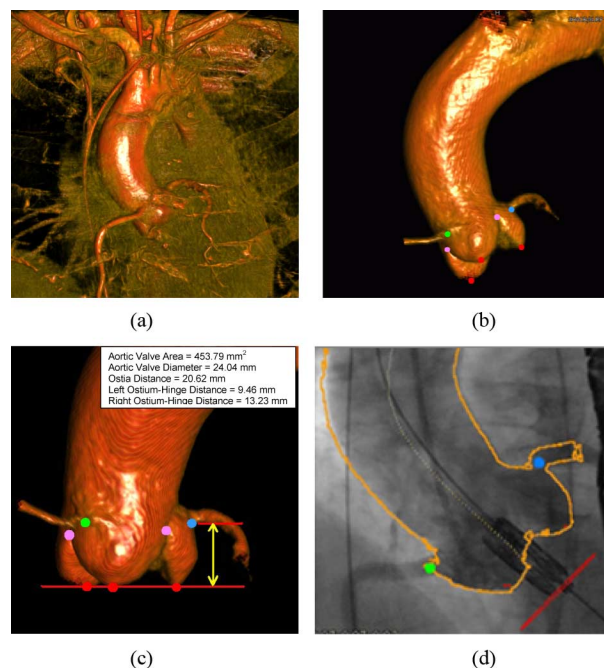

Fig. 3. Applications of C-arm CT to transcatheter aortic valve implantation. (a) A C-arm CT volume. (b) Automatically segmented aorta together with the detected valve landmarks. (c) 3-D geometric measurements of the valve. (d) Overlay of the segmented aorta onto a 2-D fluoroscopic image for visual guidance during valve deployment.

be minimized. Overlaying a patient-specific aorta model extracted from 3-D images onto real-time fluoroscopy provides valuable visual guidance to the physician. Computed tomography (CT) is often used to provide the necessary 3-D geometric measurements in pre-operative surgical planning. However, CT images are rarely used intra-operatively during valve implantation because 2-D/3-D overlay (or registration) of data captured from different imaging devices is quite difficult.

C-arm CT has recently emerged as a new imaging technique with the following advantages, compared to conventional CT. Since both the 3-D volume and 2-D fluoroscopic images are captured on the same device, overlay of the 3-D patient-specific aorta model onto a 2-D image is straightforward and accurate (except for relatively small cardiac and respiratory motion). Please refer to Section V for more detail about the 2-D/3-D overlay of the aorta model. Therefore, besides providing the 3-D valve measurements as CT, C-arm CT can be easily integrated into the intra-operative TAVI workflow to provide visual guidance. Furthermore, since C-arm CT is scanned shortly before the valve deployment (instead of days before as conventional CT), it better reflects the current state of the patient's anatomy.

In this paper, we propose robust and efficient methods for automatic aorta segmentation and aortic valve landmark detection in C-arm CT for TAVI, as shown in Fig. 3. Besides providing the aforementioned 3-D valve measurements, our system has a few specific applications to the TAVI workflow. For example, the

detected aortic hinges can be used to predict a proper C-arm angulation[1] to mitigate the foreshortening of the aorta, therefore reducing the tilting of the prosthetic valve with respect to the aortic root after deployment. Selecting a proper angulation to reduce foreshortening is important for many fluoroscopy guided interventional procedures, e.g., coronary angiography [7]–[9], and C-arm CT can also be used to reduce the overlap with other irrelevant structures of high attenuation (e.g., spine and ribs) [9]. Overlay of the detected aortic commissures helps to guide the deployment of some nonrotation-symmetric valves, which need to be aligned with the valve cusps. In summary, there are four major potential applications of the proposed automatic segmentation system in TAVI:

1) provide 3-D valve measurements for surgical planning;
2) provide a proper angulation (perpendicular to the aortic annulus) for a C-arm system;
3) provide orientation guidance for implanting prosthetic valves that are not rotation symmetric;
4) overlay of the detected coronary ostia onto 2-D fluoroscopic images provides guidance to physicians to avoid blocking the ostia after valve deployment.

Various methods have been proposed to segment the aorta. However, they work on a well established imaging modality, such as CT or magnetic resonance imaging (MRI). Automatic segmentation of the aorta in a C-arm CT volume is far more challenging. First, the image quality from different clinical sites varies quite a lot since C-arm CT is too new to have a well accepted scanning protocol. We also observed significant

---

[1]The C-arm gantry has two degrees of freedom in rotation. Angulation means the gantry orientation after combined rotation around both the primary and secondary axes.

variations inside the same clinical site since physicians were testing different scanning parameters (e.g., the amount of contrast agent and timing of the image acquisition). Conventional image processing techniques, e.g., intensity-based thresholding, region growing, and the watershed method, are usually not robust under such large variations. We propose to use machine learning techniques to exploit the rich information embedded in an expert-annotated dataset. Second, the field-of-view varies quite a lot for C-arm CT. For example, the aortic arch and descending aorta may be captured in some volumes, but missing in others. To address this challenge, we propose a part-based aorta model. The whole aorta is split into four parts: aortic root, ascending aorta, aortic arch, and descending aorta. Using the part-based model, the whole aorta does not need to be fully present. Depending on the parts that can be detected, different workflows can be exploited; therefore, a large structural variation can be elegantly handled.

Aortic valve landmarks play an important role in the surgical planning and visual guidance for TAVI. However, there is very limited work on automatic aortic valve landmark detection, except coronary ostium detection in CT angiography (CTA) for coronary analysis [10]–[14]. In this work, we detect eight important aortic valve landmarks (three hinges, three commissures, and two coronary ostia). Independent detection of each landmark [15] is not robust since some landmarks are barely visible due to imaging noise and the washout of contrast agent. The detected landmarks may be inconsistent in their relative positioning due to the lack of constraints in independent detection.

In this paper, we propose to use a hierarchical approach by first detecting a global object comprised with all eight valve landmarks. The global object is detected efficiently using the marginal space learning (MSL) method [16]. From the position, orientation, and scale of this global object, we can infer the rough position of individual landmarks. Each landmark is then refined in a small region under the guidance of its own specific landmark detector. There is no standard way to define the pose of the global object and an ad hoc solution is by no means optimal. We propose an optimization-based method to define global object pose to minimize the error of the inferred landmark position. Besides the improved robustness, our approach is also more efficient than the independent detection scheme [15].

Full automation, robustness, and efficiency are the keys for the success of a system in a real day-to-day clinical utilization. Our approach is robust under all kinds of variations observed in a real clinical setting, including changes in the field-of-view, contrast agent injection, scan timing, and aortic valve regurgitation. Taking about 1.1 s to process a volume on a computer with 2.33-GHz quad-core processors and 3 GB memory, it is much more computationally efficient than the previous work [12], [17], [18]. Automation and segmentation speed may be less of a concern for pre-operative surgical planning, but extremely important for an intra-operative application. The patient is lying on the table with many medical devices inserted (e.g., transesophageal echocardiographic transducer and various catheters). The whole surgery team (including interventional cardiologists, cardiac surgeons, nurses, and technicians, etc.) may be halted, waiting for the segmentation result. In such a clinical setting, an efficient, automatic segmentation system is

highly appreciated, being much easier to be seamlessly integrated into the workflow. Under the guidance of our system, promising outcomes have been achieved in real clinical applications. To the best of our knowledge, this is the first work to apply automatic segmentation to C-arm CT for TAVI, and our preliminary results have been published as conference papers [19], [20].

The proposed methods are built upon our previous work on MSL [16], which is applied to detect/segment the aortic root, aortic arch, and the global valve landmark object. However, besides the novel application to the TAVI procedure, this work also presents two major contributions to the detection/segmentation techniques. First, using a part-based aorta model, MSL is extended to segment the aorta under large structural variations due to the limited field-of-view. Second, a novel method is proposed to reduce the shape initialization error. After estimating the pose of the global valve landmark object using MSL, a mean shape (composed with eight valve landmarks) is aligned to the estimated pose to generate the initial position of the landmarks. In this work, we propose an optimization-based method to determine the best mean shape from a training set so that the landmark initialization error is minimized. This technique can be extended for better initialization of other nonrigid structures, e.g., heart chambers and livers.

The remainder of the paper is organized as follows. The related work on aorta segmentation and aortic valve landmark detection is reviewed in Section II. The part-based aorta modeling and segmentation is presented in Section III, followed by detailed description of the proposed aortic valve landmark detection method in Section IV. In Section V, we briefly describe how the automatic detection/segmentation is integrated in the TAVI workflow. Quantitative evaluation is performed in Section VI for the aorta segmentation, aortic valve landmark detection, and the 3-D valve measurements derived from the automatic segmentation. Furthermore, the accuracy of the imaging guidance is evaluated. This paper concludes with Section VII for discussions of the future work.

II. RELATED WORK

There is far more prior work on aorta segmentation than valve landmark detection, while the latter is dominated by the detection of coronary ostia for coronary analysis. Aorta segmentation is primarily used for aortic aneurysm analysis [21]–[33] and coronary analysis [10]–[14], though it can also be applied for aortic calcium detection [34], connective tissue disorder detection [17], blood flow quantification [35], and pulse wave velocity measurement [36], etc. Only recently, we see its application on TAVI [6], [18], [37]. Most of the proposed methods focus on one part of the aorta, e.g., the descending aorta for aneurysm analysis and the ascending aorta for coronary analysis. CT and MRI are the major imaging modalities of the aorta, with only a few exceptions using ultrasound [38] and C-arm CT [6], [37]. With a tubular shape, the aorta can be detected and segmented using generic tubular structure segmentation approaches [39]–[41] as those applied to a coronary artery, which mainly use various vesselness filters to enhance and extract the centerline, followed by lumen segmentation. Since the aorta is a much bigger structure than a coronary artery, more efficient

methods (e.g., region growing, active contours, and level sets) have been proposed to segment the lumen directly without extracting the centerline first [10], [17].

Aortic aneurysm analysis (including aneurysm detection, segmentation, measurement, stent simulation, and virtual endoscopy) is a major application of aorta segmentation in previous work. Accurate segmentation of the aorta (including the lumen and thrombus outer wall) facilitates the measuring of the maximum aneurysm diameter and thrombus volume, which are critical for a physician to decide if the patient should be treated immediately or can still be on monitoring [33]. Normally, CT angiography (CTA) is the imaging modality and only the abdominal or thoracic part of the descending aorta is segmented. The intersection of the descending aorta with a CT image slice has an elliptic shape, which is relative easy to track along slices. Compared to the thrombus outer wall, the lumen is much easier to segment in contrasted CTA images. However, most algorithms are not fully automatic and a user still needs to click at least one or two points to initialize the segmentation [24], [25]. Thrombus segmentation needs more interactive user corrections [24] or to be constrained by the segmented lumen [25].

The ascending aorta is often segmented on CTA images to detect coronary ostia, therefore providing seeds for the following coronary artery centerline extraction and lumen segmentation. Many methods require at least one user click inside the aorta to initialize the segmentation. For example, in [10], starting from a user clicked point, the aorta is segmented using a slice-by-slice region growing algorithm. It is possible to detect the intersection of the ascending aorta on each slice using a Hough transform-based circle detector, therefore making the whole procedure fully automatic [13]. To avoid leakage into the left ventricle, some heuristic rules have to be exploited to stop the region growing or circle tracking [10], [13]. To improve computational efficiency, the Hough transform is performed only once in [14] to detect a seed point, followed by region growing based tracing. Tek *et al.* [12] proposed a significantly different method for automatic aorta segmentation. The left ventricle is segmented first and used to constrain the search for the aorta. Since the left ventricle is segmented too, the whole procedure is time consuming, taking about 6.2 s on a computer with a 2.8-GHz CPU.

MRI is another important imaging modality of the aorta to detect the connective tissue disorder [17], and to measure the aorta elasticity [42], blood flow [35], and pulse wave velocity [36], etc. In these applications, the whole aorta is often presented in the volume and need to be segmented; therefore, the tortuous aortic arch needs to be handled properly [42]. Zhao *et al.* [17] proposed a semi-automatic method to segment the aorta in cine MR images. Starting from user specified seed points, a fast marching method is applied to provide an initial segmentation. The optimal surface method incorporating the motion information is developed to refine the segmentation.

Most of the previous methods are semi-automatic (a user needs to click at least one point [17]) and slow (taking up to 450 s to process one volume [40]). Furthermore, the previous work on aorta segmentation focuses on a relatively consistent imaging protocol with much fewer variations than ours. For example, a roughly same portion of the aorta is captured and the usage of contrast agent is consistent, resulting in stable image characteristics. However, our C-arm CT data exhibit large variations in both contrast agent injection and field-of-view (resulting in missing aorta part in a volume). In robust active shape models (ASM), the missing part can be treated as outliers, which are detected based on random sub-sampling [43], [44] or checking the ratio of inter-landmark distances [45]. However, the robust estimation methods have an implicit assumption that the majority of the landmarks are inliers. Therefore, the performance starts to break down quickly when the outlier ratio is more than 50% [45]. In our application, more than half of the aorta is often missing from a volume. Specific to aorta segmentation, the method proposed by Peters *et al.* [46], [47] can also handle variation in the field-of-view, where the segmented heart chambers are used to predict the initial aorta position. Therefore, one can determine which part of the aorta is presented in the volume and process it properly. However, in our application, we cannot rely on the segmentation of heart chambers since they are normally not contrasted in C-arm CT for TAVI, therefore difficult to segment.

Previous work on aortic valve landmark detection focuses on coronary ostia in CTA for coronary analysis. The process starts from segmenting the ascending aorta and a coronary artery is detected as a thin tubular structure attached to the aorta. The position of the attachment is taken as the detected ostium. For example, the largest connected components on each side of the aortic root are picked as the left and right coronary arteries in [10]. However, simple connected component analysis is not robust under imaging noise, resulting in a success rate of only 57%. Alternatively, coronary centerlines can be tracked from the aorta surface in order to detect coronary ostia [12]. Since the computationally expensive centerline tracing algorithm needs to run on the whole aorta surface, it is more time consuming. Compared to coronary ostium detection, there is less work on the detection of other aortic valve landmarks, i.e., the aortic hinges and commissures in this case. Ionasec *et al.* [48] presented a comprehensive aortic valve model, which includes all eight valve landmarks. Since the trajectory of the landmarks in the whole dynamic sequence is detected holistically, the detection accuracy on a static 3-D volume is not clear. In their early work [15], the landmarks are detected independently to each other in a static volume. Independent detection of multiple landmarks is time consuming and may result in unrealistic geometric configurations due to the lack of constraints.

With the rapid adoption of TAVI, recently, we saw some work on aorta segmentation for TAVI surgical planning [6], [18], [37], [49], [50]. For example in [18], the cardiac chambers and the aorta are segmented in pre-operative CT, and a detailed aortic valve model is proposed and integrated into the heart model. The initial position of coronary ostia is predicted from the segmented aortic valve, followed by model-based adaptation for the final detection. More closely related to our work, Gessat *et al.* [6], [37] proposed a semi-automatic method on pre-operative C-arm CT for TAVI surgical planning. The aorta is segmented using a region growing method starting from a user specified point. The coronary ostia and aortic hinges are manually labeled. The extracted aorta model is then manually aligned and overlaid onto intra-operative fluoroscopy to provide guid-
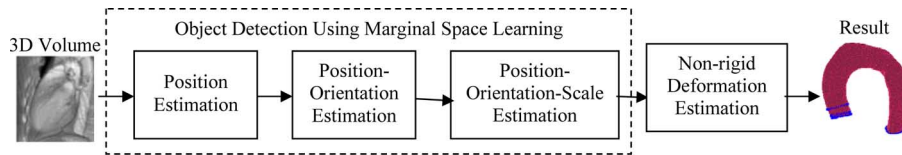
Fig. 4. Diagram of marginal space learning-based nonrigid object detection and segmentation [16].

ance. In our approach, all these steps are fully automatic and can be finished in about one second. Since the segmentation is performed on intra-operative C-arm CT, the overlay of the aorta model to fluoroscopy is also automatic using the intrinsic C-arm coordinate system.

III. PART-BASED AORTA SEGMENTATION

In this section, we first give a brief introduction of our generic 3-D object detection and segmentation method using marginal space learning (MSL) [16], which is used to segment the aortic root and aortic arch. We then present our part-based aorta detection and segmentation method in detail.

A. Marginal Space Learning for 3-D Object Segmentation

Recently, we proposed marginal space learning (MSL) [16] as an efficient and robust method for 3-D anatomical structure detection and segmentation in medical images. Here, we give a brief overview of MSL and interested readers are referred to [16] for more details. Our technique is based on recent advances in learning discriminative models to exploit rich information embedded in a large expert-annotated database. We formulate the segmentation as a two-step learning problem: anatomical structure localization and boundary delineation.

Object localization (or detection) is a prerequisite for an automatic segmentation system and discriminative learning-based approaches have proved to be efficient and robust for solving 2-D object detection problems [51]. In these methods, object detection is formulated as a classification problem: whether an image block contains the target object or not. The object pose parameter space is quantized into a large set of discrete hypotheses and exhaustive search is used to pick the best hypothesis. To be specific, each hypothesis is tested by the trained classifier to get a detection score and the hypothesis with the largest score is taken as the final detection result. To accurately localize a 3-D object, nine pose parameters need to be estimated (three for translation, three for orientation, and three for anisotropic scaling). With the exponential increase of potential pose parameter combinations, exhaustive search is not practical for 3-D object detection. The idea of MSL is not to learn a classifier directly in the full similarity transformation space but to incrementally learn classifiers on marginal spaces. In our case, we split the estimation into three steps: position estimation, position-orientation estimation, and position-orientation-scale estimation. After each step, we only keep a small number of promising hypotheses; therefore, the pose parameter space is pruned significantly to increase the detection efficiency.

After objection detection, we get the position, orientation, and scale of the object. The mean shape is aligned to the estimated transformation to get a rough estimate of the object shape. We then deform the shape to fit the object boundary. Active shape models (ASM) [52] are widely used to deform an initial estimate of a nonrigid shape under the guidance of image evidences and shape prior. The nonlearning-based generic boundary detector in the original ASM [52] is not robust under complex background or weak edges. We use a learning-based method to exploit more image evidences to achieve robust boundary detection. Fig. 4 shows the system diagram for MSL-based nonrigid object detection and segmentation.

MSL provides a generic framework for automatic object detection and segmentation. Its efficiency can be further boosted by exploiting the prior constraints among the pose parameters in the marginal spaces [53], resulting in detection speed of less than a second for most applications. MSL has been successfully applied to many 3-D anatomical structure detection and segmentation problems in all major medical imaging modalities [53], e.g., livers in abdominal CT, and heart chambers in both CT and ultrasound images.

B. System Diagram for Part-Based Aorta Segmentation

Due to the variation in the field-of-view, the aorta in a C-arm CT volume has no consistent structure; therefore, our MSL-based approach cannot be applied directly. In this paper, we propose a part-based aorta model (as shown in Fig. 5) by splitting the whole aorta into four parts: aortic root, ascending aorta, aortic arch, and descending aorta. The aortic root and aortic arch are consistent in anatomy; therefore, we can apply MSL to train two separate detectors with one for each. The length of the ascending and descending aorta parts varies; therefore, we use a tracking-based method to handle this variation. Fig. 6 shows the system diagram of the proposed part-based aorta segmentation method. We first detect the aortic root since it should always be present in the volume. The aortic arch detector is then applied. If the aortic arch is not presented, therefore, not detected, the descending aorta is often also missing in the volume.[2] We track the ascending aorta starting from the aortic root until the top volume border. If the aortic arch is detected, we track the ascending aorta starting from the aortic root until the arch. We also track the descending aorta downward from the arch if the arch is detected. After tracking, we get the centerline of the whole aorta and a tube is synthesized as an initial rough estimate of the shape. We then adjust each mesh point along the surface normal to an optimal position, which has the largest response from a learning-based boundary detector. Generic mesh smoothing [54] is applied to enforce the smoothness constraint.

---

[2]Volumes with missing aortic arch are reconstructed with slice size of 256×256 pixels, instead of 512×512 pixels The slice resolution is roughly the same, resulting in a much smaller trans-axial field-of-view. Therefore, the descending aorta is also outside the volume.
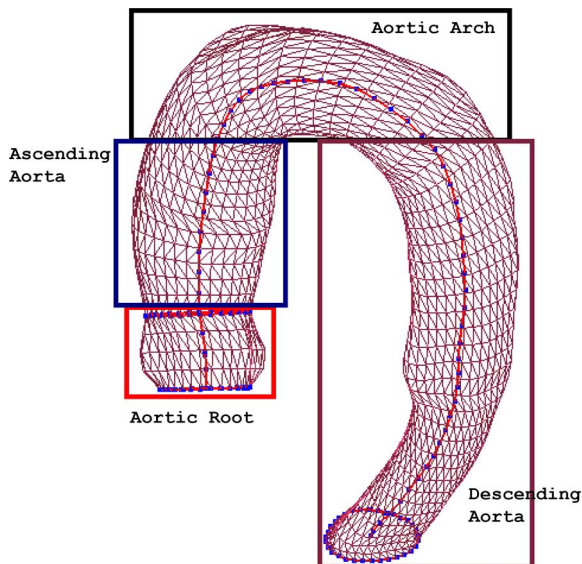
Fig. 5. Part-based aorta model. The whole aorta is split into four parts, namely aortic root, ascending aorta, aortic arch, and descending aorta.
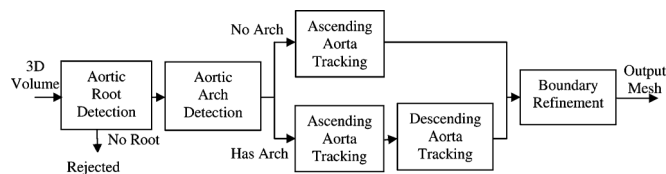

Fig. 6. System diagram for part-based aorta segmentation.

Mesh point adjustment and mesh smoothing can be iterated a few times to improve the boundary delineation accuracy.

C. Aortic Root Segmentation

In anatomy, the aortic root refers to the aorta segment between the aortic hinges and the sinotubular junction. Previous non-model-based approaches [10], [13], [14] have difficulty to exactly delineate the boundary between the aortic root and the left ventricular outflow tract (LVOT) since they are fully connected and both contrasted in CTA. In C-arm CT, the contrast agent is directly applied to the aortic root; therefore, the boundary is clear if the aortic valve is fully closed. However, due to the aortic valve regurgitation, the contrast agent may leak into the LVOT in about 20%–30% of cases. The amount of leakage varies depending on the severity of the regurgitation, which creates an extra challenge to an automatic segmentation method. As a consistent anatomy, the aortic root is segmented using MSL in our system by fitting a surface mesh model into the data. Fig. 7 shows the aortic root segmentation results on a few data, demonstrating the robustness of MSL under the variations of contrast agent and aortic valve regurgitation. The contrast of the first volume is strong (though with some imaging artifacts presented around the aortic root), while the second volume has quite weak contrast. The amount of regurgitation also varies quite a lot from no regurgitation [Fig. 7(a)] to severe regurgitation [Fig. 7(d)].
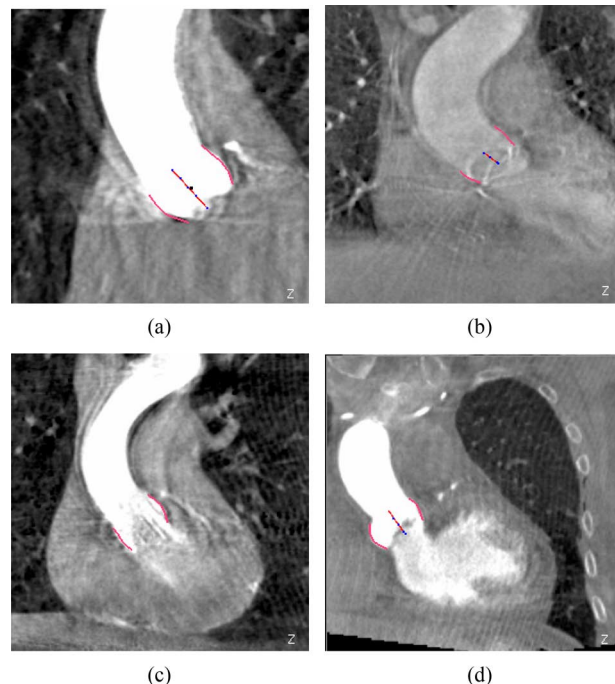

Fig. 7. Aortic root segmentation results under the variations of contrast agent and aortic valve regurgitation.

D. Aortic Arch Segmentation

The aortic arch is missing in about half of our dataset due to the limited field-of-view of the C-arm CT; therefore, the missing or presence of the aortic arch needs to be detected automatically. Since the aorta has a tubular shape, the intersection perpendicular to its centerline is close to a circle. A tracking-based approach is often used to trace the circular shape, which works well on the ascending and descending aorta parts. However, the aorta centerline orientation needs to be estimated and updated robustly during the tracking of the bending arch [42]. Otherwise, a tracking error may be propagated to the following slices, resulting in a failure (e.g., tracing into the supra-aortic arteries or the nearby pulmonary artery). In this paper, we treat the aortic arch as a holistic anatomical structure. In our part-based aorta model (Fig. 5), the aortic arch is defined as the part from the top of the aorta to the axial slice where the intersection of the aorta diverges into two separated parts. As the case of the aortic root, MSL is applied to detect and segment the aortic arch. By segmenting the bending aortic root and arch with a model-based approach, the remaining parts are much easier to handle. Since the intersection of the ascending and descending aorta parts to an axial slice is close to a circle, it can be tracked efficiently without estimating the centerline orientation.

E. Tracking of Ascending and Descending Aorta Parts

The length of the visible ascending and descending aorta parts varies significantly from volume to volume. Consequently, we propose to use a tracking technique to deal with this variation. After excluding the aortic arch, which is detected with MSL, the remaining aorta has a close to circular shape on the trans-axial intersection. Instead of using a time-consuming Hough transform based circle detector [13], [14], we use machine learning
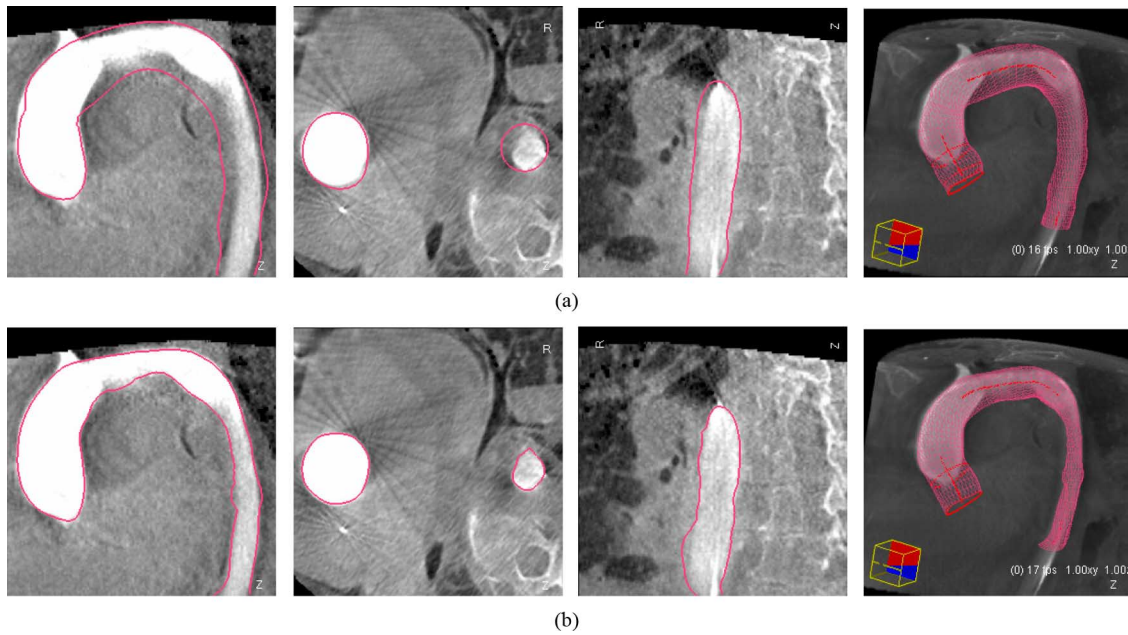
Fig. 8. Aorta boundary refinement. (a) Initial synthesized tubular mesh after tracking the ascending and descending aorta parts. (b) Final segmentation after boundary refinement. The first three columns show three orthogonal cuts of the volume and the last column shows the corresponding 3-D meshes.

technique to train a 2-D circle detector on an axial image slice using 2-D Haar wavelet features [51]. Though the part close to the bottom of the aortic arch has a more elliptical shape, the deviation from a circle is still well constrained. Trained on all such intersections, our circle detector is robust, though the circle is a less accurate approximation of a more elliptical shape. The tracking of the ascending aorta starts from the top of the aortic root and is performed slice by slice, moving toward the patient's head. The detected circle on a slice is propagated to the next slice and the circle detector is applied in a neighborhood of 6×6 mm^2 around the initial estimate. For an image slice containing the ascending aorta, normally, the detector may find multiple circle candidates around the true position. We pick the one closest to the circle on the previous slice. If the aortic arch is detected in the volume, the tracking procedure stops on the slice touching the aortic arch. Otherwise, it stops when no aortic circles are detected or it reaches the top volume border. Tracking of the descending aorta is quite similar. The aortic arch is a bended tube with two arms, one for the ascending aorta and the other for the descending aorta. Tracking of the descending aorta starts from the topmost axial slice touching the descending arm of the aortic arch. The intersection of the already segmented aortic arch mesh on that slice provides the initial position of the descending aorta. The same procedure (as the tracking of the ascending aorta) is then used to track the descending aorta slice-by-slice towards the patient's abdomen. The tracking stops on the slice with no aortic circles detected or reaching the bottom volume border.

Slice-by-slice tracing is less robust than the MSL-based global object detection. In this application, it is sufficient for the ascending aorta, which is short and well constrained by the aortic root at the bottom and the aortic arch at the top. However, the tracking error of the descending aorta may build up since it is a very long tubular structure. In addition, the contrast agent inside the descending aorta is often pretty weak and gradually washes out. Most of the aorta segmentation error comes from the descending aorta. Fortunately, the descending aorta is less important than the other parts in guiding the TAVI procedure. Therefore, the clinical requirement of the segmentation accuracy is less strict.

F. Aorta Boundary Refinement

After tracking the ascending and descending aorta parts, we get the centerline of the whole aorta. A generalized-cylinder model is synthesized as an initial estimate of the aorta shape and the radius at each centerline point is set to the radius of the detected circle. Fig. 8(a) shows the synthesized tube after tracking. The initialization is close to the true aorta boundary; however, a circle does not fit the boundary exactly. A learning-based boundary detector is exploited for final boundary delineation. Interested readers are referred to [16] for more details of the learning-based boundary detector. One difference to the boundary delineation of the aortic root or arch is that we cannot use the active shape models (ASM) to enforce prior shape constraint since the aorta is not consistent in structure due to the variation in the field-of-view. Instead, a generic mesh smoothing technique [54] is used to achieve a smooth surface for the segmented aorta. To be specific, a two-step iterative approach is used.

1) Use the learning-based boundary detector to adjust each mesh point along the surface normal to the optimal position where the response of the boundary detector is the largest.
2) Apply generic mesh smoothing.

The above two steps are iterated a couple of times to improve the boundary delineation accuracy. Fig. 8(b) shows the result after boundary refinement. More examples of the aorta segmentation results are shown in Fig. 9.

Note that, almost all previous work uses bottom-up approaches [11], [17], [39], [40], [42] to track the aorta centerline
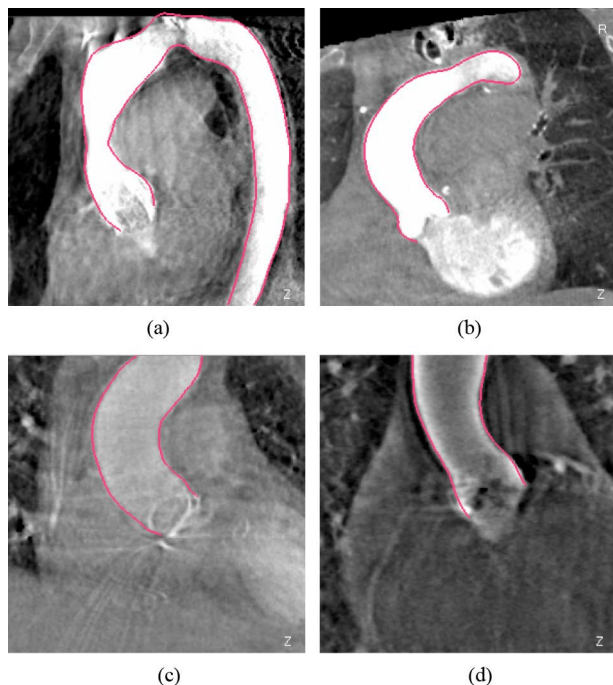
Fig. 9. Automatic aorta segmentation on a few example volumes. (a) Good contrast in the whole aorta. (b) Severe aortic valve regurgitation. (d) Low contrast. (d) Contrast agent is almost washed out due to bad timing.

to handle variations. They are neither automatic nor robust to noisy images. In comparison, we use the top-down MSL [16] to detect the aortic root and arch, and use bottom-up tracking to detect ascending and descending aorta parts, which have large variations in length. Our system is a nice combination of both approaches.

IV. AORTIC VALVE LANDMARK DETECTION

Besides segmenting the aorta, we detect eight aortic valve landmarks (see Fig. 1), i.e., three aortic hinges, three aortic commissures, and left and right coronary ostia, since they are important in both surgical planning and providing visual guidance during valve deployment. Though it is possible to detect each landmark independently [15], the detection results may be inconsistent in geometry. It also wastes computational power by ignoring the strong geometric constraint among the landmarks. We propose an efficient hierarchical approach by first detecting a global object comprised with all eight valve landmarks. From the position, orientation, and scale of this global object, we can infer the rough position of individual landmarks. Each landmark is then refined in a small region (e.g., a cube of 10 mm centered on the initial position) under the guidance of its own specific landmark detector.

A. Optimal Mean Shape for Accurate Shape Initialization

Similar to aortic root detection, we use marginal space learning (MSL) [16] to efficiently detect the position, orientation, and scale of the global landmark object. For a learning-based method, we need to specify the ground truth of object pose for each training volume; thereby, a learning algorithm can learn the implicit relationship between the image and object pose, which is later used to infer the correct pose

from an unseen volume. However, there is no standard way to define the pose of the global object containing eight landmarks. After detecting the global landmark object, we align the mean shape (which is the average shape of the training set after global transformation has been compensated) to the global pose to get an initial estimate of each individual landmark's position. This initialization needs to be accurate. Otherwise, the final boundary evolution may get stuck in a wrong position due to the complication of the surrounding tissues. The mean shape is generally calculated as an average of the normalized shapes in an object-centered coordinate system. Therefore, the optimal mean shape and optimal pose definition are closely related. In [16], the orientation of a heart chamber is defined by its long axis; the position and scale are determined by the oriented bounding box of the chamber surface mesh. Although working well in applications with relatively small shape variations, the mean shape derived using the oriented-bounding-box based method is not optimal at all.

In this paper, we present an approach to searching for an optimal mean shape $\bar{m}$ that can represent the whole population well. A group of training shapes, $M_1, M_2, \ldots, M_N$ are supposed to be given and each shape is represented by J points M_i^j, $j = 1, \ldots, J$ ($J = 8$ for the aortic valve landmarks). The optimal mean shape $\bar{m}$ should minimizes the residual errors after alignment

$$\bar{m} = \arg\min_m \sum_{i=1}^{N} \|\mathcal{T}_i(m) - M_i\|^2. \tag{1}$$

Here, $\mathcal{T}_i$ is the corresponding transformation from the mean shape $\bar{m}$ to each individual shape M_i. This procedure is called generalized Procrustes analysis [55] in the literature. An iterative approach can be used to search for the optimal solution. We first randomly pick an example shape as a mean shape. We then align each shape to the current mean shape. The average of the aligned shapes (the simple average of the corresponding points) is calculated as a new mean shape. The iterative procedure converges to a locally optimal solution after a few iterations.

The similarity transformation with isotropic scaling is often used as the transformation $\mathcal{T}$. However, MSL can efficiently estimate anisotropic scales of an object. By removing more deformations, the shape space after alignment is more compact and the mean shape can represent the whole population more accurately. Therefore, we use an anisotropic similarity transformation to represent the transformation between two shapes, i.e., $\mathcal{T}$ represents translation ($T = [X, Y, Z]'$), rotation (represented as a rotation matrix R), and anisotropic scaling (S_x, S_y, S_z). The transformation of a 3-D point P is

$$\mathcal{T}(P) = R \begin{bmatrix} S_x & 0 & 0 \\ 0 & S_y & 0 \\ 0 & 0 & S_z \end{bmatrix} P + T. \tag{2}$$

The optimal $\mathcal{T}$ to align two shapes m and M is

$$\hat{T}, \hat{R}, \hat{S}$$
$$= \arg\min_{T,R,S} \sum_{j=1}^{J} \left\| \left(R \begin{bmatrix} S_x & 0 & 0 \\ 0 & S_y & 0 \\ 0 & 0 & S_z \end{bmatrix} m^j + T \right) - M^j \right\|^2. \tag{3}$$

Suppose there is a common scale $s = (S_x + S_y + S_z)/3$, and let $S'_x = S_x/s$, $S'_y = S_y/s$, and $S'_z = S_z/s$. Equation (3) can be rewritten as

$$\hat{T}, \hat{R}, \hat{S}$$
$$= \arg \min_{T,R,S} \sum_{j=1}^{J} \left\| \left(Rs \begin{bmatrix} S'_x & 0 & 0 \\ 0 & S'_y & 0 \\ 0 & 0 & S'_z \end{bmatrix} m^j + T \right) - M^j \right\|^2. \tag{4}$$

Since there are no closed-form solutions for estimating the anisotropic similarity transformation, we propose a two-step iterative approach to searching for the optimal transformation.

1) Starting from the given anisotropicity (S'_x, S'_y, S'_z), we estimate the similarity transformation with isotropic scaling, (T, R, s).
2) With the given similarity transformation (T, R, s), we update the anisotropicity (S'_x, S'_y, S'_z).

In the first step, at beginning, we can assume the scaling is isotropic, $S'_x = 1$, $S'_y = 1$, and $S'_z = 1$. The isotropic similarity transformation can be estimated using a closed-form solution [55, p. 84]. After some mathematical derivations, we find that the second step also has a closed form solution as follows:

$$\hat{S}'_x = \frac{\sum_{j=1}^{J} m^j(x) Q^j(x)}{\sum_{j=1}^{J} m^j(x)^2}$$

$$\hat{S}'_y = \frac{\sum_{j=1}^{J} m^j(y) Q^j(y)}{\sum_{j=1}^{J} m^j(y)^2}$$

$$\hat{S}'_z = \frac{\sum_{j=1}^{J} m^j(z) Q^j(z)}{\sum_{j=1}^{J} m^j(z)^2} \tag{5}$$

where

$$Q^j = \frac{1}{s} R^{-1} (M^j - T). \tag{6}$$

Since each step reduces the residual shape error after alignment, the process converges. In practice, it converges quickly in three to five iterations.

With a module solving the anisotropic similarity transformation between two shapes, we can plug it into the generalized Procrustes analysis method to search for the optimal mean shape $\bar{m}$. Besides the optimal mean shape, the optimal alignment $\mathcal{T}_i$ from the mean shape to each training shape is also obtained. The transformation parameters of the optimal alignment provide the pose ground truth that MSL can learn to estimate.

B. Unique Mean Shape for Aortic Valve Landmarks

The optimal mean shape $\bar{m}$ is not unique. Any translation, rotation, and scaling of $\bar{m}$ is also an optimum since the transformation of the mean shape can be compensated by the individual transformation $\mathcal{T}_i$. We remove the unnecessary flexibility of the mean shape using the oriented-bounding-box based approach [16] as follows. We first define a unique orientation. Suppose three aortic hinges are denoted as H_1, H_2, and H_3; three aortic commissures are denoted as C_1, C_2, and C_3; and O_l and O_r represent the left and right coronary ostium, respectively. Let $H_c = (H_1 + H_2 + H_3)/3$ be the mass center of three aortic hinges and $C_c = (C_1 + C_2 + C_3)/3$ be the mass center of three aortic commissures. The z axis is defined as a unit vector pointing from the hinge center H_c to the commissure center C_c

$$z = \frac{C_c - H_c}{\|C_c - H_c\|}. \tag{7}$$

The x axis is derived as follows:

$$x_1 = \frac{O_r - O_l}{\|O_r - O_l\|} \tag{8}$$

$$x_2 = (z \times x_1) \times z \tag{9}$$

$$x = \frac{x_2}{\|x_2\|}. \tag{10}$$

Here, initial axis x_1 is defined as a unit vector pointing from the left coronary ostium O_l to the right coronary ostium O_r. We then rotate the x_1 axis inside the plane spanned by the x_1 and z axes to make it perpendicular to the z axis, arriving axis x_2. The final x axis is achieved by normalizing x_2 to a unit vector. The y axis is then a cross product of the z and x axes, $y = z \times x$.

After defining the orientation of the global shape, we calculate an oriented bounding box for the eight landmarks. We set the origin of the object-centered coordinate system to the center of the box. We scale the bounding box anisotropically to make it a cube of 1 mm in length. The optimal mean shape $\bar{m}$ is tightly bounded in the cube. After each iteration of the generalized Procrustes analysis, $\bar{m}$ is normalized using the above procedure, therefore uniquely defined. We would like to emphasize that such normalization of the mean shape $\bar{m}$ does not change its optimality, but helps to achieve a unique solution.

C. Efficient Hierarchical Aortic Valve Landmark Detection

On our evaluation dataset with 278 volumes (see Section VI-A), the mean landmark error [the Euclidean distance defined in (3)] inferred from the aligned mean shape is about 2.77 mm using the oriented-bounding-box based approach. The Procrustes analysis converges after three iterations and the mean landmark error is significantly reduced to 1.90 mm. It demonstrates that the optimal mean shape derived using the proposed method can better represent the whole shape population. Fig. 10(a) and (b) show the distribution of the aligned landmarks using the oriented-bounding-box based approach and the proposed optimization approach, respectively. It is clear that the distribution is more compact using the proposed method.

After inferring the initial landmark position from the pose of the detected global object, each landmark is then refined in a small region (e.g., a cube of 10 mm centered on the initial position) under the guidance of its own specific landmark detector. Trained with the probabilistic boosting tree classifier, our landmark detector is similar to the detector used by Ionasec *et al.* [48], but using the steerable features [16] that can be efficiently extracted from the original volume. On the contrary, the method
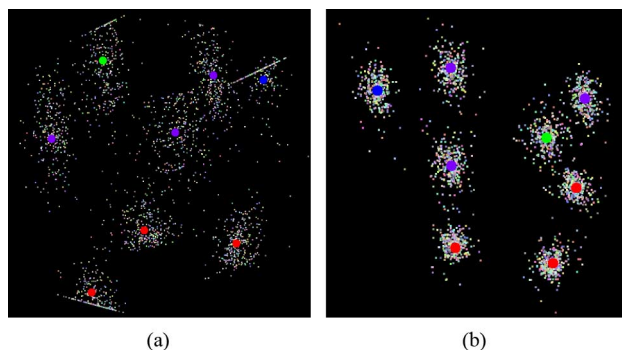
Fig. 10. The aligned of aortic valve landmarks and mean shape (represented as big circles) using (a) the oriented-bounding-box based approach [16] and (b) the proposed optimization approach.
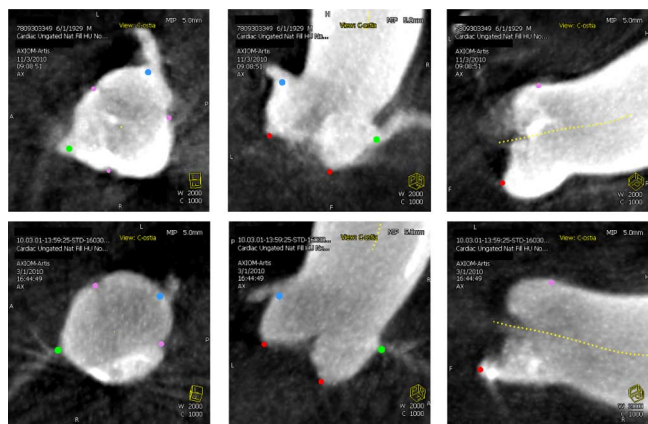

Fig. 11. The aortic valve landmark detection results on two example data with red dots for the hinges, purple for the commissures, blue for the left coronary ostium, and green for the right coronary ostium. Each row shows three orthogonal cuts of a volume.

of Ionasec *et al.* needs to resample the original volume to an isotropic resolution (e.g., 1 mm) to use the Haar wavelet features. Fig. 11 shows the detected aortic valve landmarks after local refinement on two example volumes.

V. WORKFLOW INTEGRATION FOR TAVI

In this section, we describe the integration of the automatic aorta segmentation and aortic valve landmark detection into the TAVI workflow. We follow the steps the system performs during the valve deployment and discuss the potential user interactions. All described components have been integrated into an angiographic C-arm system (Artis zee/zeego with Siemens syngo Workplace, Erlangen, Germany). Right before the implantation, the physician starts to obtain a 3-D C-arm CT volume of the aortic root by acquiring a rotational 2-D image sequence of $200°$ over 5 s on the C-arm system. Via a pigtail catheter, 15–25 ml contrast agent (diluted to 75 ml) is injected over 5 s (with a 1-s X-ray delay) into the aortic root. To minimize the respiratory motion artifact, the physicians temporally stop mechanical ventilation to the patient. Furthermore, rapid ventricular pacing[3] is applied to a heart rate that yields no effective heart pumping and minimal blood flow. This allows using a relatively small

---

[3]Rapid pacing is regarded as a safe procedure by many physicians. However, a few physicians have concern that rapid pacing may peel off some cardiac calcifications into the blood circulation, raising the risk of strokes.
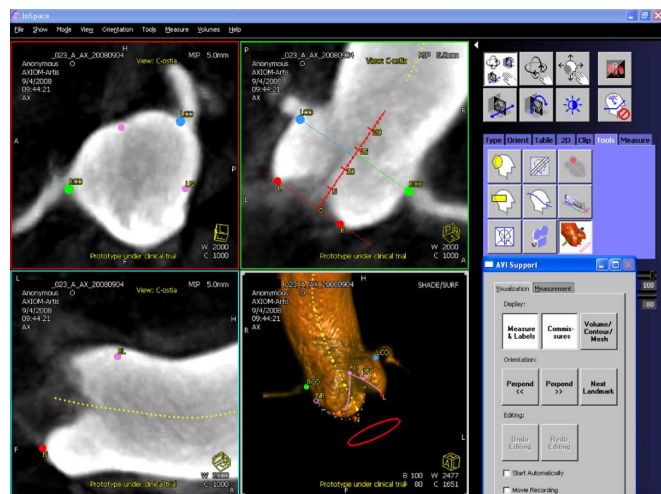

Fig. 12. Screen shot of our prototype. Detected landmarks (coronary ostia in blue and green, commissures in purple, hinges in red, centerline in yellow) and derived structures (perpendicularity circle and ruler in red) are shown in 3-D volume rendering and three orthogonal intersection planes with 15 mm slice thickness. The panel in the lower right shows the user interface we added to the existing system.

amount of contrast agent, compared to approximately 80 ml for a conventional CT and approximately 15 ml for a single 2-D angiogram [56]. After the rotational run is finished on the C-arm system, all of the following steps 1–5 are started and performed fully automatically.

1) Reconstructing 3-D CT volume from acquired rotational image sequence.

The 3-D volume is reconstructed based on a software available with the angiographic C-arm system [57], which takes about 12 s.

2) Segmenting the aorta and detecting the aortic valve landmarks from 3-D volume.

The proposed method is applied to segment the aorta and detect eight aortic valve landmarks: the aortic hinges that are the lowest points of aortic root cusps (to support finding a C-arm angulation perpendicular to the aortic root), the coronary artery ostia (which have to stay open after prosthesis implantation), and the aortic commissures where the cusps meet (to help orienting anatomically designed valve prostheses). The aorta centerline is also calculated from the segmented aorta mesh. This process is quite fast, taking about 1 s.

3) Deriving additional structures from detected landmarks.

We derive a circle parallel to the plane spanned by the three aortic hinges (see the red circle in the bottom-right quadrant of Fig. 12). Visually, this perpendicularity circle degenerates to a straight line if and only if the three aortic hinges are aligned [see Fig. 13(a)], which corresponds to a perpendicular angulation for valve implantation. It is important to avoid tilting of the deployed prosthetic valve with respect to the aortic root (i.e., the centerline of the prosthetic valve should be aligned accurately to the centerline of the aortic root) to minimize the postprocedure complications (e.g., valvular regurgitation and aortic root rupture) [3]. The tilting inside the imaging plane is relatively easy to correct by the physician during prosthetic valve positioning under the guidance of fluoroscopy. The out-of-plane tilting is avoided if both the aortic root and the prosthetic valve have no
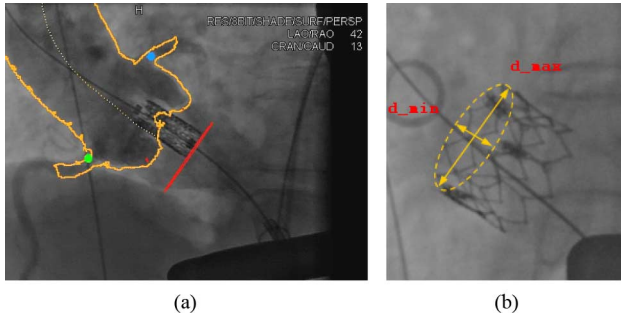
Fig. 13. Evaluation of imaging guidance in the TAVI workflow. (a) Overlay with almost perfect matching. (b) Measurement of potential tilting of the prosthesis (for better illustration we show an image from an angulation not used for valve deployment).

foreshortening on the imaging plane. The metal frame of a prosthetic valve is clearly visible under fluoroscopy, therefore, can be adjusted to avoid tilting by checking the top or bottom ring of the prosthesis [see Fig. 13(b)]. However, it is much more difficult to find a proper angulation for the aortic root. As soft tissue, the aortic root is not visible under fluoroscopy and contrast agent needs to be injected to check the foreshortening. Previously, multiple iterations of adjustments need to be performed, composed with 1) injecting contrast to check the foreshortening, 2) determining the next angulation to try, and 3) rotating the C-arm to that angulation. Using our system, the physician can perform virtual rotations to get a proper angulation (on which the derived perpendicularity circle degenerates into a straight line) and, once done, the C-arm can automatically rotate to the selected angulation. Additionally, contrast injections for perpendicularity checks can be avoided in this process.

To estimate the likelihood for the coronary ostia to stay open after implantation, the physician wants to measure their distance to the aortic hinge plane. We create a ruler orthogonal to that plane (see the red ruler in the top-right quadrant of Fig. 12). We decided to show a ruler instead of numbers, because this makes the measurement process transparent to the physician and allows for user compensation of the measurement in case of misdetected landmarks. The coronary artery dilates to a funnel shape around its ostium, with a diameter up to 5 mm. Traditionally, the ostium landmark is put at the center of the funnel shape (as we did in this work), while some physicians may prefer to put the ostium landmark at the bottom edge close to the aortic hinge plane to get a more conservative distance measurement. A ruler gives the physicians flexibility to adjust the measurement based on their own preference.

4) Extract interior of segmented aortic shape out of 3-D volume for volume rendering.

The interior of the segmented aorta is extracted from the volume and visualized with volume rendering. Visualization of coronary arteries is also important, but automatic segmentation is difficult. To make them visible without segmenting them explicitly, we add voxels within 15 mm (determined heuristically) to each detected coronary ostium into volume visualization.

5) Computing optimized volume rendering transfer function parameters.

We want to avoid letting the user find manually the appropriate volume rendering parameters c_{opt} for transfer function

center and w_{opt} for transfer function width. Therefore, they are calculated automatically based on the voxel intensities

$$c_{opt} = f_{c,in}m_{in} + f_{c,out}m_{out} + f_{c,offset}, \qquad (11)$$

$$w_{opt} = f_{w,in}m_{in} + f_{w,out}m_{out} + f_{w,offset}. \qquad (12)$$

Here, m_{out} (m_{in}) is a volume specific value and is determined by the mean intensity of all voxels outside (inside) the boundary of the segmented aorta with a fixed distance to it. The six parameters $f_{c,in}$, $f_{c,out}$, $f_{w,offset}$, $f_{w,out}$, $f_{w,offset}$ are tuned on a few training data.

6) Landmark verification or correction.

The automatically detected valve landmarks need to be verified by the physicians, and corrected if necessary (though it rarely happens in practice). To give the physicians a good initial view, the volume is centered and zoomed based on the position of the two detected coronary ostia and as many landmarks as possible are shown on the three orthogonal volume intersection planes (see Fig. 12).

If landmark positions and visualization are satisfactory, the physician can perform the following steps.

7) Rotating 3-D volume to an appropriate C-arm angulation.

Every rotation of the volume rendering view corresponds to a C-arm angulation (up to in-plane rotation). Therefore, using the displayed perpendicularity circle or the commissures, the physician can virtually choose a view that corresponds to an appropriate C-arm angulation. The system then allows automatically rotating the C-arm to that angulation.

8) Overlay of 3-D structures onto fluoroscopic images.

The live overlay [see Fig. 13(a)] of the rendered 3-D visualization onto fluoroscopic images is based on software available with the angiographic C-arm system. The 3-D volume is inherently registered to the fluoroscopic images because both images are acquired on the same system. The information of any further C-arm rotations and table movements is fed to our application and the overlay can be dynamically adapted. The adaptation step is purely based on the machine coordinate system; therefore, it is robust and fast. However, it does not compensate for patient and cardiac/respiratory motions, which is part of our future work.

VI. EXPERIMENTS

In this section, we quantitatively evaluate the accuracy of aorta segmentation and aortic valve landmark detection on a large diverse C-arm CT dataset. Effectiveness of the C-arm CT-based imaging guidance system in the real TAVI workflow is also evaluated, including the aorta model overlay accuracy and the tilting of the deployed prosthetic valve.

A. Evaluation of Aorta Segmentation and Valve Landmark Detection

We collected a dataset of 319 C-arm CT volumes from 276 patients from 11 clinical sites over the world (mainly from Germany, Australia, Japan, Canada, and USA). Most patients have only one C-arm CT volume. If the image quality of the first C-arm CT is not good enough, the physicians may perform another C-arm CT scan. It normally happens on the first few cases from a new clinical site with limited experience in C-arm CT. Therefore, those patients may have up to three volumes

TABLE I
AORTIC VALVE LANDMARK DETECTION ERRORS BASED ON A FOUR-FOLD CROSS-VALIDATION ON 278 VOLUMES.THE MEAN,
STANDARD DEVIATION (STD), AND MEDIAN OF THE ERRORS ARE REPORTED (MEASURED IN MILLIMETERS)

	Aortic Hinges			Coronary Ostia			Aortic Commissures		
	Mean	STD	Median	Mean	STD	Median	Mean	STD	Median
After Global Pose Estimation	3.38	1.27	3.16	4.26	1.78	4.01	3.35	1.31	3.18
After Local Refinement	2.09	1.18	1.82	2.07	1.53	1.61	2.17	1.31	1.88

TABLE II
ERRORS OF SELECTED AUTOMATIC 3-D MEASUREMENTS BASED ON A FOUR-FOLD CROSS-VALIDATION ON 278 VOLUMES, INCLUDING THE ERROR
OF THE DISTANCE MEASUREMENT (IN MILLIMETERS) FROM CORONARY OSTIA TO THE AORTIC HINGE PLANE, AND THE ANGLE (IN DEGREES)
BETWEEN THE DETECTED AND TRUE AORTIC HINGE PLANE NORMALS

	Left Ostium to Hinge Dist.			Right Ostium to Hinge Dist.			Hinge Plane Normal		
	Mean	STD	Median	Mean	STD	Median	Mean	STD	Median
Measurement Errors	2.10	1.86	1.73	2.51	2.03	2.11	3.68°	3.61°	2.73°

with variations in contrast agent injection and scan timing. In our early collection, 15 patients also have a C-arm CT right after the prosthesis deployment for post-deployment evaluation, e.g., measuring valve regurgitation. Six patients have prosthetic valves implanted from previous open-heart surgery. The aortic hinges of the native valve have been destroyed on all the postdeployment C-arm CT. The size of each slice in a volume is 256×256 or 512×512 pixels. A volume contains around 200–300 slices. The image resolution is isotropic and varies from volume to volume in the range of $[0.70, 0.84]$ mm.

A four-fold cross-validation is performed to evaluate our algorithm. The whole dataset is randomly split into four roughly equal sets. Three sets are used to train the system and the remaining set is reserved for testing. The configuration is rotated, until each set has been tested once.

The aorta segmentation accuracy is measured using the symmetric point-to-mesh distance [16]. For each point on a mesh, we search for the closest point on the other mesh to calculate the minimum distance. We calculate the point-to-mesh distance from the detected mesh to the ground-truth and vice versa to make the measurement symmetric. The contrast agent gradually fades out along the descending aorta; therefore, the length of the segmented aorta may differ from the manual annotation since it is difficult to determine consistently where the segmentation should stop. When we calculate the error between the segmented mesh and the ground truth, we exclude the extra distal part of the descending aorta from evaluation. On average, the length of the excluded part is about 35 mm, which corresponds to about 15% of the descending aorta. The mean segmentation error of the remaining aorta is 1.08 mm, with a standard deviation of 0.56 mm. Fig. 9 shows aorta segmentation results on a few volumes. The proposed method is robust under the variations of the field-of-view, contrast agent, scan timing, and valve regurgitation.

We also quantitatively evaluate the valve landmark detection accuracy. The post-deployment C-arm CT (15 volumes) is excluded since the native aortic hinges have been destroyed and the aortic commissures have been significantly deformed. The patients (six volumes) with prosthetic valves implanted from previous open-heart surgery are excluded for the same reason. We also exclude a few volumes (20 volumes) with extremely poor image quality that the landmarks cannot be identified even by an expert (though the aorta can be successfully segmented on

these volumes). Fig. 7(b) shows an example volume excluded in the evaluation of landmark detection. For these patients, a second C-arm CT scan with better image quality is available, which is used to guide the TAVI procedure.

A four-fold cross-validation is performed on the remaining 278 volumes for aortic valve landmark detection. The landmark detection accuracy is measured using the Euclidean distance from the detected landmark to the ground truth. Table I shows the detection errors. After global landmark object pose estimation, we can get a good initial estimate of the landmark position. The mean errors range from 3.35 to 4.26 mm for different landmarks. Compared to the aortic hinges and commissures, the initial coronary ostia have a larger mean error of 4.26 mm due to the larger variations in the origin of a coronary artery. After local refinement for each landmark, the errors are significantly reduced. For example, the mean error of the aortic hinges reduces from 3.38 mm to 2.09 mm. The coronary ostia achieve the largest reduction in detection error, from 4.26 mm to 2.07 mm. Fig. 11 shows the detected valve landmarks in two typical volumes.

Multiple 3-D valve measurements can be derived from the segmentation results. Due to the space limit, we only evaluate the error in measuring the distance from the left and right coronary ostia to the aortic hinge plane. As shown in Table II, the mean error for measuring the left coronary ostium to hinge plane distance is 2.10 mm. The right coronary ostium has a larger mean error of 2.51 mm. The overall distance measurement error is only slightly larger than the landmark detection errors (2.07 mm for the coronary ostia and 2.09 mm for the aortic hinges). The aortic hinge plane normal (calculated from the detected aortic hinges) plays an important role in selecting a proper C-arm angulation, which can affect the tilting of the deployed prosthetic valve; therefore, it needs to be estimated accurately. We calculate the angle between the estimated hinge plane normal and its true value derived from the ground truth. As shown in Table II, the mean angle is 3.68°. A tilting error of 5° is regarded by physicians as almost perfect (Section VI-B). Our error is within this range, therefore can meet the clinical requirement.

Regarding the segmentation accuracy, we cannot compare our error with those reported in the literature directly because they used different datasets captured from different imaging modalities. Most of the previous aorta segmentation methods

TABLE III
COMPARISON WITH PREVIOUS AORTA SEGMENTATION METHODS WITH REPORTED QUANTITATIVE MESH ERRORS

	Modality	Patients/ Subjects	Volumes	Resolution (mm)	Automatic	Speed	Mesh Error
Zhao *et al.* [17]	MRI	104	16-25 volumes/subject	$1.5 \times 1.5 \times 1.5$ to $2.0 \times 2.0 \times 2.0$	No	5 min/subject	1.55 mm
Bruijne *et al.* [40]	CT	23	2 volumes/subject	$0.448 \times 0.448 \times 2.0$	No	450 s/volume	1.4 mm[a]
Waechter *et al.* [18]	CT	20	1 volume/subject	N/A	Yes	N/A	0.5 mm[b]
Proposed Method	C-arm CT	276	319 volumes in total	0.70-0.84 isotropic	Yes	0.8 s/volume	1.08 mm

[a] If an aortic aneurysm presents, the outer wall of the aneurysm is segmented, which is more difficult than the aorta lumen.
[b] The mesh error includes the aortic root and the valve leaflets.

did not present a quantitative evaluation of the segmentation accuracy [6], [11], [14], [21], [36], [38] or reported in different error criteria [29], [31], [35], [42]. Table III lists the reported aorta mesh errors available in the literature. Roughly, our accuracy is comparable to the state-of-the-art, e.g., 1.55 mm reported in [17] on 104 MRI datasets, 1.4 mm reported in [40] on 23 CT datasets, and 0.5 mm reported in [18] on 20 CT datasets. Most of the previous work on aortic valve landmark detection focuses on coronary ostia to initialize the tracing of coronary arteries in CTA [10]–[14]. In that application, the detection accuracy is measured as how many coronary arteries have been successfully traced and no quantitative distance measurements are reported. In [15], all eight aortic valve landmarks are detected and the overall landmark detection error is 2.28 mm on CT data, which is comparable to ours. In [18], Waechter *et al.* reported smaller errors in aorta segmentation and valve landmark detection. For example, the detection error of the left and right coronary ostia are 1.0 and 1.2 mm, respectively, resulting is correspondingly smaller 3-D measurement errors (0.6–0.9 mm for ostia-to-hinge-plane distance and 1.8° for hinge plane normal error). The errors are evaluated on a small CT dataset with 20 volumes and one volume with failed coronary ostium detection is excluded. For comparison, we do not exclude any detection outliers. Normally, a cardiac CT has a higher resolution (often around 0.3–0.4 mm for in-slice resolution) than our C-arm CT (0.70–0.84 mm). Unfortunately, Waechter *et al.* did not report the volume resolution of their dataset. If standard high-resolution cardiac CT is used in [18] and the errors are measured in voxels, our accuracy in aorta segmentation and landmark detection is comparable to [18].

Our approach is computationally efficient, taking about 1.1 s (0.8 s for aorta segmentation and 0.3 s for valve landmark detection) to process a volume on a computer with 2.33 GHz quad-core processors and 3 GB memory. It is at least 10 times faster than the previous methods [12], [17].

B. Evaluation of Imaging Guidance in TAVI Workflow

In the following experiments, we evaluate the accuracy of our imaging guidance system in patients who received an Edwards Sapien valve prosthesis (Edwards Lifesciences, Irvine, CA). These valves are deployed under rapid ventricular pacing. Retrospectively, we analyze the first 20 cases that were supported by our system and where the overlay image scene was documented. We first evaluate the accuracy of the overlay of the 3-D model and the X-ray images. We assume that a misalignment corresponds to a shift parallel to the projection plane,

which simplifies the evaluation but ignores rotations. For each patient, we take an image from the recorded overlay scene that showed a contrast injection with rapid pacing right before deployment of the prosthesis [see Fig. 13(a)]. We then measure the shift error as the distance (in pixels) of a landmark point (e.g., an aortic hinge or coronary ostium) that could be identified in the X-ray image and 3-D overlay. Furthermore, we measure the shift along the aortic root centerline, which is the most important direction for guiding the implantation. Because of the projective geometry of the images, a measurement in pixels must be scaled using the known length of an object in approximately the same distance to the X-ray detector. For this, we use the known length of the implanted prosthesis (in mm) divided by its measured height (in pixels). For the 20 evaluated patients, we get a shift error of 3.1 ± 1.9 mm (mean $\pm$ standard deviation) and in centerline direction a shift error of 1.9 ± 1.5 mm. The reasons for pronounced deviation in a few patients could be the dislocation of the aortic root by sheath-manipulation and accidentally movements of the patients caused by the physician. The measured accuracy is only valid under repeat rapid pacing, which recovers the heart position that we had during the 3-D imaging; therefore, the influence of cardiac motion is minimized.

We are also interested in how well the system can help to position the valve in the aortic root anatomy with minimal tilting. Since a C-arm angulation suggested by our system influences the final valve tilting, it would be interesting to evaluate the post-deployment valve position in the patient anatomy. Unfortunately, this would require a postoperative C-arm CT scan, incurring additional contrast agent injection and X-ray dose; therefore, it is not done for most patients. (The 15 postdeployment volumes in our dataset were captured before the development of our system. Since the valve deployment was not guided by our system, we could not use them to evaluate the tilting.) Instead, we determine for each patient the tilting angle of the implanted prosthesis in the 2-D fluoroscopic image under the chosen angulation. Thereby, we assume the tilting inside the imaging plane has been corrected by the physician during prosthesis positioning right before the deployment, as discussed in Step 3 of the TAVI workflow in Section V; therefore, ideally, a proper angulation would result in a valve image not showing any tilting. With this assumption, we also ignore other factors like the complex interaction of operators, devices, and patient anatomy. We measure the minimum and maximum elliptical diameters of the upper prosthesis ring in the image in pixels [see Fig. 13(b)] and derive the tilting by $90° - acos(d_{\min}/d_{\max})$. This value says how perpendicular the valve prosthesis is imaged right after implantation. For the 20 evaluated patients, we

get a tilting of $5.7° \pm 5.2°$ (mean $\pm$ standard deviation). Clinically, a tilting of less than $5°$ can be stated as very good (obtained in 60% of the patients in our study), $5°–10°$ as good (30%), $10°–15°$ as acceptable (5%), and larger than $15°$ as inappropriate (5%). The values show that a procedure with C-arm CT support by our system yields overall good results. Reasons for suboptimal angulation estimation may be due to the extra dislocation of the aortic root after C-arm CT scan and/or accidental patient movements.

VII. CONCLUSION AND FUTURE WORK

In this paper, we presented a fully automatic aorta segmentation and valve landmark detection system in C-arm CT with applications to transcatheter aortic valve implantation (TAVI). The system is very fast, on average, taking only 1.1 s to process a volume. It is fully automatic and robust under all kinds of variations observed in a real clinical setting, including changes in the field-of-view, contrast agent injection, scan timing, and aortic valve regurgitation. In practice, landmark adjustments are only rarely done by the user. The initial clinical trials have demonstrated the usefulness of our system in the TAVI workflow, e.g., providing a proper angulation to avoid large tilting of a prosthetic valve after deployment. Hundreds of TAVI procedures have been performed with our system and live demos have been presented at several clinical conferences [58]–[60].

A valuable extension of our system would be the integration of preoperative conventional CT images into the TAVI workflow. Our segmentation approach is generic, therefore can be extended easily to other imaging modalities by simple retraining, without any manual parameter tuning. A similar automatic detection and segmentation system has been built on cardiac CT data for surgical planning. Robust 2-D/3-D registration of the CT model onto real-time fluoroscopy is required to use CT for visual guidance. An automatic registration algorithm has been proposed and the preliminary results are promising [61]. Currently, it is under system integration for clinical evaluation.

REFERENCES

[1] F. T. Billings, S. K. Kodali, and J. S. Shanewise, "Transcatheter aortic valve implantation: Anesthetic considerations," *Anesthesia Analgesia*, vol. 108, no. 5, pp. 1453–1462, 2009.

[2] M. B. Leon *et al.*, "Transcatheter aortic-valve implantation for aortic stenosis in patients who cannot undergo surgery," *N. Eng. J. Med.*, vol. 363, no. 17, pp. 1597–1607, 2010.

[3] P. Schoenhagen, J. Hausleiter, S. Achenbach, M. Y. Desai, and E. M. Tuzcu, "Computed tomography in the evaluation for transcatheter aortic valve implantation (TAVI)," *Cardiovasc. Diagnosis Therapy*, vol. 1, no. 1, pp. 44–56, 2011.

[4] M. J. Mack, "Does transcatheter aortic valve implantation mean the end of surgical aortic valve replacement," *Texas Heart Inst. J.*, vol. 37, no. 6, pp. 658–659, 2010.

[5] C. R. Smith *et al.*, "Transcatheter versus surgical aortic-valve replacement in high-risk patients," *N. Eng. J. Med.*, vol. 364, no. 23, pp. 2187–2198, 2011.

[6] M. Gessat, D. R. Merk, V. Falk, T. Walther, S. Jacobs, A. Nöttling, and O. Burgert, "A planning system for transapical aortic valve implantation," *Proc. SPIE Med. Imag.*, vol. 7261, 2009.

[7] S.-Y. J. Chen, J. D. Carroll, and J. C. Messenger, "Quantitative analysis of reconstructed 3-D coronary arterial tree and intracoronary devices," *IEEE Trans. Med. Imag.*, vol. 21, no. 7, pp. 724–740, Jul. 2002.

[8] O. Wink, R. Kemkers, S.-Y. J. Chen, and J. D. Carroll, "Intra-procedural coronary intervention planning using hybrid 3-dimensional reconstruction techniques," *Acad. Radiol.*, vol. 10, no. 12, pp. 1433–1441, 2003.

[9] J. A. Garcia, B. Movassaghi, I. P. Casserly, A. J. Klein, S.-Y. J. Chen, J. C. Messenger, A. Hansgen, O. Wink, B. M. Groves, and J. D. Carroll, "Determination of optimal viewing regions for X-ray coronary angiography based on a quantitative analysis of 3-D reconstructed models," *Int. J. Cardiovas. Imag.*, vol. 25, no. 5, pp. 455–462, 2009.

[10] A. Hennemuth, T. Boskamp, D. Fritz, C. Kühnel, S. Bock, D. Rinck, M. Scheuering, and H.-O. Peitgen, "One-click coronary tree segmentation in CT angiographic images," *Proc. Comput. Assist. Radiol. Surg.*, pp. 317–321, 2005.

[11] S. C. Saur, C. Kühnel, T. Boskamp, G. Székely, and P. Cattin, "Automatic ascending aorta detection in CTA datasets," in *Proc. Workshop Bildverarbeitung für der Medizin*, 2008, pp. 323–327.

[12] H. Tek, M. A. Gulsun, S. Laguitton, L. Grady, D. Lesage, and G. Funka-Lea, "Automatic coronary tree modeling," *Insight J.*, 2008.

[13] C. Wang and O. Smedby, "An automatic seeding method for coronary artery segmentation and skeletonization in CTA," *Insight J.*, 2008.

[14] S. Wang, L. Fu, Y. Yue, Y. Kang, and J. Liu, "Fast and automatic segmentation of ascending aorta in MSCT volume data," in *Proc. Int. Conf. Image Signal Process.*, 2009, pp. 1–5.

[15] R. Ionasec, B. Georgescu, E. Gassner, S. Vogt, O. Kutter, M. Scheuering, N. Navab, and D. Comaniciu, "Dynamic model-driven quantification and visual evaluation of the aortic valve from 4D CT," in *Proc. Int. Conf. Med. Image Computing Computer Assist. Intervent.*, 2008, pp. 686–694.

[16] Y. Zheng, A. Barbu, B. Georgescu, M. Scheuering, and D. Comaniciu, "Four-chamber heart modeling and automatic segmentation for 3-D cardiac CT volumes using marginal space learning and steerable features," *IEEE Trans. Med. Imag.*, vol. 27, no. 11, pp. 1668–1681, Nov. 2008.

[17] F. Zhao, H. Zhang, A. Wahle, M. T. Thomas, A. H. Stolpen, T. D. Scholz, and M. Sonka, "Congenital aortic disease: 4D magnetic resonance segmentation and quantitative analysis," *Med. Image Anal.*, vol. 13, no. 3, pp. 483–493, 2009.

[18] I. Waechter, R. Kneser, G. Korosoglou, J. Peters, N. H. Bakker, R. v. d. Boomen, and J. Weese, "Patient specific models for planning and guidance of minimally invasive aortic valve implantation," in *Proc. Int. Conf. Med. Image Computing Computer Assisted Intervent.*, 2010, pp. 526–533.

[19] Y. Zheng, M. John, R. Liao, J. Boese, U. Kirschstein, B. Georgescu, S. K. Zhou, J. Kempfert, T. Walther, G. Brockmann, and D. Comaniciu, "Automatic aorta segmentation and valve landmark detection in C-arm CT: Application to aortic valve implantation," in *Proc. Int. Conf. Med. Image Computing Computer Assisted Intervent.*, 2010, pp. 476–483.

[20] M. John, R. Liao, Y. Zheng, A. Nöttling, J. Boese, U. Kirschstein, J. Kempfert, and T. Walther, "System to guide transcatheter aortic valve implantations based on interventional 3-D C-arm CT imaging," in *Proc. Int. Conf. Medical Image Computing Computer Assist. Intervent.*, 2010, pp. 375–382.

[21] S. Loncaric, M. Subasic, and E. Sorantin, "3-D deformable model for aortic aneurysm segmentation from CT images," in *Annu. Int. Conf. IEEE Eng. Med. Biol. Soc.*, 2000, pp. 398–401.

[22] M. Subasic, D. Kovacevic, S. Loucaric, and E. Sorantin, "Segmentation of abdominal aortic aneurysm using deformable models," *Proc. East West Vision*, pp. 61–66, 2002.

[23] M. de Bruijne, B. van Ginneken, W. J. Niessen, M. Loog, and M. A. Viergever, "Model-based segmentation of abdominal aortic aneurysms in CTA images," *Proc. SPIE Med. Imag.*, vol. 5032, pp. 1560–1571, 2003.

[24] M. de Bruijne, B. van Ginneken, M. A. Viergever, and W. J. Niessen, "Interactive segmentation of abdominal aortic aneurysms in CTA images," *Med. Image Anal.*, vol. 8, no. 2, pp. 127–138, 2004.

[25] S. D. Olabarriaga, J.-M. Rouet, M. Fradkin, M. Breeuwer, and W. J. Niessen, "Segmentation of thrombus in abdominal aortic aneurysms from CTA with non-parametric statistical grey level appearance modeling," *IEEE Trans. Med. Imag.*, vol. 24, no. 4, pp. 477–485, Apr. 2005.

[26] K. J. Kirchberg, A. Wimmer, and C. H. Lorenz, "Modeling the human aorta for MR-driven real-time virtual endoscopy," in *Proc. Int. Conf. Medical Image Computing Computer Assist. Intervent.*, 2006, pp. 470–477.

[27] T. Kovács, P. Cattin, H. Alkadhi, and S. W. Székel, "Automatic segmentation of the vessel lumen from 3-D CTA images of aortic dissection," in *Proc. Workshop Bildverarbeitung für der Medizin*, 2006, pp. 161–165.

[28] T. Kovács, P. Cattin, H. Alkadhi, and S. W. Székel, "Automatic segmentation of the aortic dissection membrane from 3-D CTA images," *Proc. Med. Imag. Augment. Reality*, pp. 317–324, 2006.

[29] V. Galante, C. Corsi, F. Veronesi, V. Russo, R. Fattori, and C. Lamberti, "Dynamic characterization of aorta morphology and function in presence of an aneurysm," *Proc. Comput. Cardiol.*, vol. 34, pp. 765–678, 2007.

[30] J. Egger, T. O'Donnel, C. Hopfgartner, and B. Freisleben, "Graph-based tracking method for aortic thrombus segmentation," in *Proc. Eur. Conf. Int. Fed. Med. Biol. Eng.*, 2008, pp. 584–587.

[31] J. Egger, B. Freisleben, R. Setser, R. Renapuraar, C. Biermann, and T. O'Donnel, "Aorta segmentation for stent simulation," in *Proc. MICCAI Workshop Cardiovas. Intervent. Imag. Biophys. Model.*, London, U.K., 2009, pp. 1–10.

[32] J. Dehmeshki, H. Amin, M. Ebadian-Dehkordi, A. Jouannic, and S. Qanadi, "Automatic detection, segmentation and quantification of abdominal aortic aneurysm using computed tomography angiography," *Proc. Med. Image Understand. Anal.*, pp. 32–36, 2009.

[33] C. Kauffmann, A. Tang, A. Dugas, E. Therasse, V. Oliva, and G. Soulez, "Clinical validation of a software for quantitative follow-up of abdominal aortic aneurysm maximal diameter and growth by CT angiography," *Eur. J. Radiol.*, vol. 77, pp. 502–508, 2011.

[34] U. Kurkure, O. C. Avila-Montes, and I. A. Kahadiaris, "Automated segmentation of thoracic aorta in non-contrast CT images," in *Proc. IEEE Int. Symp. Biomed. Imag.*, 2008, pp. 29–32.

[35] A. O. Al-Agamy, N. F. Osman, and A. S. Fahmy, "Segmentation of ascending and descending aorta from magnetic resonance flow images," in *Cairo Int. Biomed. Eng. Conf.*, 2010, pp. 41–44.

[36] S. S. Giri, Y. Ding, A. Nishijima, A. Pedraza-Toscano, P. M. Burns, R. L. Hamlin, and O. P. Simonetti, "Automated and accurate measurement of aortic pulse wave velocity using magnetic resonance imaging," *Proc. Comput. Cardiol.*, vol. 34, pp. 661–664, 2007.

[37] M. E. Karar, M. Gesset, T. Walther, O. Falk, and O. Burgert, "Towards a new image guidance system for assisting transapical minimally invasive aortic valve implantation," in *Proc. Ann. Int. Conf. IEEE Eng. Med. Biol. Soc.*, 2009, pp. 3645–3648.

[38] K. Krissian, J. Ellsmere, K. Vosburgh, R. Kikinis, and C.-F. Westin, "Multiscale segmentation of the aorta in 3-D ultrasound images," in *Proc. Annu. Int. Conf. IEEE Eng. Med. Biol. Soc.*, 2003, pp. 638–641.

[39] T. Behrens, K. Rohr, and H. H. Stiehl, "Robust segmentation of tubular structures in 3-D medical images by parametric object detection and tracking," *IEEE Trans. Syst., Man, Cybern. B*, vol. 33, no. 4, pp. 554–561, Aug. 2003.

[40] M. de Bruijne, B. van Ginneken, M. A. Viergever, and W. J. Niessen, "Adapting active shape models for 3-D segmentation of tubular structures in medical images," *Proc. Inf. Process. Med. Imag.*, pp. 136–147, 2003.

[41] D. Lesage, E. D. Angelini, I. Bloch, and G. Funka-Lea, "A review of 3-D vessel lumen segmentation techniques: Models, features and extraction schemes," *Med. Image Anal.*, vol. 13, no. 6, pp. 819–845, 2009.

[42] D. Rueckert, P. Burger, S. M. Forbat, R. D. Mohiaddin, and G. Z. Yang, "Automatic tracking of the aorta in cardiovascular MR images using deformable models," *IEEE Trans. Med. Imag.*, vol. 16, no. 5, pp. 581–590, Oct. 1997.

[43] M. Rogers and J. Graham, "Robust active shape model search," in *Proc. Eur. Conf. Comput. Vis.*, Copenhagen, Denmark, 2002, pp. 517–530.

[44] S. Sun, C. Bauer, and R. Beichel, "Automated 3-D segmentation of lungs with lung cancer in CT data using a novel robust active shape model approach," *IEEE Trans. Med. Imag.*, vol. 31, no. 2, pp. 449–460, Feb. 2012.

[45] K. Lekadir, R. Merrifield, and G.-Z. Yang, "Outlier detection and handling for robust 3-D active shape model search," *IEEE Trans. Med. Imag.*, vol. 26, no. 2, pp. 212–222, Feb. 2007.

[46] J. Peters, O. Ecabert, C. Lorenz, J. von Berg, M. J. Walker, T. B. Ivanc, M. Vembar, M. E. Olszewski, and J. Weese, "Segmentation of the heart and major vascular structures in cardiovascular CT images," *Proc. SPIE Med. Imag.*, vol. 6914, 2008.

[47] O. Ecabert, J. Peters, M. J. Walker, T. Ivanc, C. Lorenz, J. von Berg, J. Lessick, M. Vembar, and J. Weese, "Segmentation of the heart and great vessels in CT images using a model-based adaptation framework," *Med. Image Anal.*, vol. 15, no. 6, pp. 863–876, 2011.

[48] R. I. Ionasec, I. Viogt, B. Georgescu, Y. Wang, H. Houle, F. Vega-Higuera, N. Navab, and D. Comaniciu, "Patient-specific modeling and quantification of the aortic and mitral valves from 4D cardiac CT and tee," *IEEE Trans. Med. Imag.*, vol. 29, no. 9, pp. 1636–1651, Sep. 2010.

[49] M. V. Navkar, E. Yeniaras, D. J. Shah, N. V. Tsekos, and Z. Deng, "Extracting geometric features of aortic valve annulus motion from dynamic MRI for guiding interventions," in *Proc. IEEE Int. Symp. Biomed. Imag.*, 2011, pp. 1302–1305.

[50] H. E. Karar, M. John, D. Holzhey, V. Falk, F. Mohr, and O. Burgert, "Model-updated image-guided minimally invasive off-pump transcatheter aortic valve implantation," in *Proc. Int. Conf. Med. Image Computing Computer Assist. Intervent.*, 2011.

[51] P. Viola and M. Jones, "Rapid object detection using a boosted cascade of simple features," in *Proc. IEEE Conf. Comput. Vis. Pattern Recognit.*, 2001, pp. 511–518.

[52] T. F. Cootes, C. J. Taylor, D. H. Cooper, and J. Graham, "Active shape models—their training and application," *Comput. Vis. Image Understand.*, vol. 61, no. 1, pp. 38–59, 1995.

[53] Y. Zheng, B. Georgescu, H. Ling, S. K. Zhou, M. Scheuering, and D. Comaniciu, "Constrained marginal space learning for efficient 3-D anatomical structure detection in medical images," in *Proc. IEEE Conf. Comput. Visi. Pattern Recognit.*, 2009, pp. 194–201.

[54] "Optimal surface smoothing as filter design," in *Proc. Eur. Conf. Comput. Vis.*, 1996, pp. 283–292.

[55] I. L. Dryden and K. V. Mardia, *Statistical Shape Analysis*. New York: Wiley, 1998.

[56] J. Kempfert, V. Falk, G. Schuler, A. Linke, D. R. Merk, F. W. Mohr, and T. Walther, "Dyna-CT during minimally invasive off-pump transapical aortic valve implantation," *Ann. Thorac Surg.*, vol. 88, no. 6, p. 2041, 2009.

[57] M. Zellerhoff, B. Scholz, E.-P. Ruehrnschopf, and T. Brunner, "Low contrast 3-D reconstruction from C-arm data," *Proc. SPIE Med. Imag.*, vol. 5745, pp. 646–655, 2005.

[58] in *23rd Annu. Meeting Eur. Assoc. Cardio-Thoracic Surg.*, Vienna, Austria, Oct. 17–21, .

[59] in *59th Annu. Sci. Session Am. College Cardiol.*, Atlanta, GA, Mar. 13–16, 2010.

[60] in *23rd Annual Scientific Symposium of Transcatheter Cardiovascular Therapeutics*, San Francisco, CA, Nov. 7–11, 2011.

[61] S. Miao, R. Liao, and Y. Zheng, "A hybrid method for 2-D/3-D registration between 3-D volumes and 2-D angiography for trans-catheter aortic valve implantation (TAVI)," in *Proc. IEEE Int. Symp. Biomed. Imag.*, 2011, pp. 1215–1218.